Hindawi
Journal of Sensors
Volume 2022, Article ID 8793615, 10 pages
https://doi.org/10.1155/2022/8793615

*Research Article*

# Monitoring Stress State of H-Shape Steel Using Ceramic Piezoelectric Sensor: A Feasibility Study

**Daopei Zhu**,[1] **Jiafeng Li**,[1] **and Zhangli Wang**[2]

[1]*School of Civil and Surveying & Mapping Engineering, Jiangxi University of Science and Technology, Nanchang 330013, China*
[2]*Gansu Construction Investment (Holdings) Group Corporation Limited, Lanzhou 730030, China*

Correspondence should be addressed to Zhangli Wang; zhangli.wang@hotmail.com

Received 7 May 2022; Revised 25 October 2022; Accepted 15 November 2022; Published 24 November 2022

Academic Editor: Tomasz Wandowski



To monitor the stress state and yield capacity of H-beams across their entire service process, a real-time monitoring method based on the energy signal response of ceramic piezoelectric sensors is proposed in this paper. The method is applied to conduct loading experiments on H-beams under different load values and web heights. Then, the amplitude and energy of the piezoelectric signals under the two working conditions are compared and analyzed, and the finite element analysis results are verified. The experimental results show that the time-domain waveform energy index increases under an increase in web height or load. Taking the H-section steel member with a web height of 10 cm as an example, when the load value is less than 500 kN/m, the energy index increases (on average) by ~10.5% for every 100 kN/m load increase; when the load value exceeds 500 kN/m and is below 675 kN/m (yield load), the same load increases the energy index by ~13.4%. Meanwhile, a 1 cm average increase in web height increases the energy index by ~14.6%. The finite element simulation results indicate that the ceramic piezoelectric sensor load increases under external load increases up to the yielding load. Because the stress state at the sensor location directly determines the stress wave propagation, the critical buckling loads of H-beams can be predicted using the energy index.

## 1. Introduction

Steel is one of the most important building materials currently available, owing to its low weight, high strength, high energy consumption capacity, and good assembly properties under earthquake action; thus, it is widely used in the construction of large span, high-rise buildings. At the same time, the lower weight ratio can reduce the sizes of beams and columns in the steel frame. In long span and high-rise structures, welded H-beams are usually used. Numerous scholars at home and abroad have carried out relevant research work on H-beams and achieved important research results. Cao and Feng et al. [1, 2] conducted experimental studies on H-shaped steel beams welded with corrugated webs and holes webs, respectively; they mainly analyzed the influence of the relevant web changes upon the shear capacities and flexural performances of H-beams. Lee et al. [3, 4] measured and calculated the shear buckling coefficient of the webs of I-beams via experiments and finite element simulations, and they analyzed the shear bearing capacity of such beams. Ellobody [5] analyzed the I-beams previously tested by Zirakian and Showkati [6], determined their buckling modes and moment values through eigenvalue buckling analysis, and then applied these values to nonlinear displacement analyses to obtain the beams' load-displacement curves. The aforementioned research and analysis regarding I- and H-beam webs have been conducted under specific experimental conditions. However, the field use process of H-beams is more complex than such specific conditions, and the shear stress in H-beams is primarily carried by the H-beam web. Therefore, it is particularly important to monitor the stress of H-beams, to ensure the safety of the entire structure.

At the same time, structural health monitoring technology has become an increasingly important research topic in the economic maintenance of infrastructure [7–10]. Because of the unique aspects of H-beam working environments, monitoring can only be performed via nondestructive testing. The application of acoustic emission technology [11–13] provides

a method for the early damage detection and real-time monitoring of structures. Most of the current acoustic emission monitoring research focuses upon structures with simple geometries or restricted areas; however, the acoustic emission source positioning strategy for actual engineering structures is fairly complex. Based on the finite element simulation results of Lamb waves, Cheng et al. [14] proposed a real structure source location method based on artificial neural networks to determine the damage and damage locations of H-shaped rigid beams. Nick et al. [15] et al. performed continuous intelligent health monitoring of steel girder bridges using a modal strain energy damage index method and an artificial neural network. Tohidi and Sharifi [16] used an artificial neural network system to predict the buckling deformation strength of I-beams in the inelastic range. Zhou, Glisic, and Raeisi et al. used distributed sensors (smart film, optical fiber sensors, and binary crack sensors, respectively) to monitor the health status of the structure [17–19]. Although many of these techniques are highly accurate and efficient, most are computationally expensive. The choice of sensor technology depends on the characteristics of the system under study. Ceramic piezoelectric materials have been widely applied as actuators and sensors for health monitoring, owing to their advantages of low cost, fast response, and embeddability [20–23].

In this paper, a method based upon a ceramic piezoelectric sensor is proposed to monitor the stress and ultimate bearing capacity of H-beams. During the experiment, the signal responses of different components were monitored using ceramic piezoelectric sensors; then, an energy index was established to measure the stress state of the H-beams. By comparing the signal response under different web heights and load conditions, the signal change rule was analyzed. In this study, an innovative health monitoring method is proposed to evaluate the stress state of an H-beam. The method can monitor this stress state nondestructively. Furthermore, it can nondestructively evaluate whether the H-beam reaches its ultimate bearing capacity and subsequently judge its safety.

## 2. Monitoring Principle and Algorithm

*2.1. Principle of H-Beam Web Strain as Studied by Ceramic Piezoelectric Sensor (PZT).* Lead zirconate titanate (PZT) is a popular piezoelectric material. It generates a charge under external stress (positive piezoelectric effect) and strain under an applied electric field (inverse piezoelectric effect). From previous studies, it is known that the induced voltage is proportional to the stress on the PZT sensor [24, 25]. The PZT-5H is a ceramic piezoelectric offering a high sensitivity, electromechanical coupling coefficient, medium constant, and flexibility; hence, it is often used to detect signals with high-frequency components [26, 27], such as ultrasonic waves [28] and shock or shock-induced stress waves [29]. In this paper, a PZT-5H ceramic piezoelectric plate was used for stress monitoring of an H-beam; the relevant parameters are shown in Table 1. The size of the PZT patch was 10 mm × 10 mm × 0.3 mm; its detailed structure and connections are shown in Figure 1.

Table 1: Material properties of PZT-5H.

| Property | Value |
|---|---|
| Density (kg/m$^3$) | 7600 |
| Electromechanical coupling factor (kP) | 0.6 |
| Piezoelectric constant $d_{33}$(CN$^{-1}$) | $4 \times 10^{-10}$ |
| Poisson ratio | 0.35 |
| Mechanical quality factor (Qm) | 80 |
| Relative permittivity ($\varepsilon_{r33}/\varepsilon_0$) | 1600 |
| Dielectric loss (tan$\delta$) | 0.025 |
| Curie temperature (°C) | 360 |
| Young's modulus($10^9$ N/m$^2$) | 117 |

A schematic diagram of the experiment is shown in Figure 2. The welded H-beam specimens were placed on the electrohydraulic servo test machine (100 tons) for fixed loading when required. The PZT piece on the left side of the H-section web was connected to a signal generator. The PZT piece on the right of the H-beam web was connected to a signal receiver. In this experiment, the signal receiver used an INV306U signal acquisition instrument to record the signal; this signal was collected and analyzed in a signal analysis software system (Coinv Dasp 2006 Professional Signal Analysis and Processing Software). The signal emitter was a DG1022U Signal Generator.

An active-sensing approach with piezoceramic sensor was utilized to monitor the stress and buckling load of H-beam. Two PZT patches were used with one as an actuator and the other as a sensor. The actuator has the capacity to generate a stress wave that will propagate through the H-beam, and the sensor will detect the propagated stress wave. The wave propagation will be influenced by the stress state of the web between the actuator and the sensor. For example, the increase of load will lead to a tighter combination between the iron atoms of the web, and the signal emitted by the signal generator attenuates less during propagation. Because of the different attenuation of the stress wave signal under different web height and different load conditions, different signal changes are produced. Through the analysis of the received signal, the stress and buckling load of H-beam can be judged.

*2.2. Basic Principles of Time-Domain Analysis.* The test wave signal is very sensitive when passing through the stressed H-beam, and it can exhibit marked signal change. In this study, the signal received by the PZT chip was investigated using the time-domain analysis method. The stress and critical load of the H-beam were monitored by calculating the energy of the signal. The proposed health monitoring algorithm defined the energy index $E$ of the signal, where$X_i$ represents a set of discrete data for the PZT-sensor-measured signal in the $i$ -th sampling, and $x_{ij}$ represents the sensor voltage at the $j$ -th sampling point in the $i$ -th sampling. The sampling time was fixed at 0.1 s. In each sampling duration, a total of $m$ sampling points were involved in the

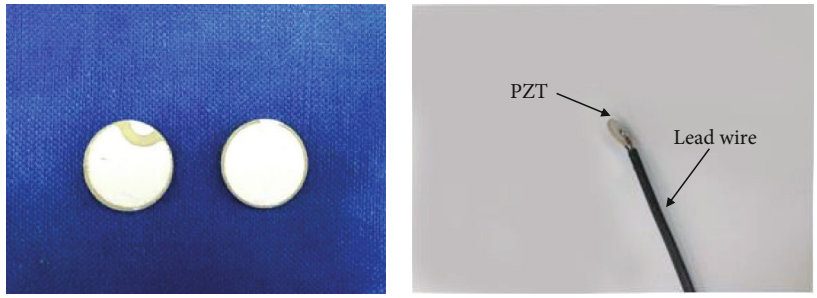


(a) (b)

Figure 1: (a) PZT-5H ceramic piezoelectric sheet and (b) a ceramic piezoelectric plate connected to a wire.

calculation. $\bar{x}_i$ denotes the average of these sampling points, and $X_i$ can be expressed by

$$X_i = (x_{i1}, x_{i2}, \cdots, x_{im}), (i = 1, 2, \cdots). \quad (1)$$

To monitor the stress and critical loads of H-beams, the energy index was defined as

$$E_i = S_i^2 = \left[\int |x_{ij}| dt\right]^2, (j = 1 \cdots m). \quad (2)$$

The value of energy index $E_i$ can be used to indicate the stress of the H-beam. Environmental noise had little effect on the test; hence, it was neglected. For example, because PZT performance is considerably influenced by ambient temperature, the modal frequency of the PZT thickness direction increases when the temperature increases. Therefore, the ambient temperature was kept at 20°C, to reduce the effects of environmental temperature. In this experiment, ceramic piezoelectric sensors are used to monitor the stress and yield capacity of H-beams.

## 3. Experiment

*3.1. Experimental Facility.* In the position of H-beam sticking point, the surface of H-section steel specimen is polished by grinding wheel to remove the rust layer on the surface of steel bar and keep the polished surface smooth. Before pasting the piezoelectric ceramic sensor, the position of the measuring point is wiped with cotton ball dipped in alcohol to remove the dirt on the surface. After the surface is dried, the piezoelectric ceramic sensor connected to the wire is pasted onto the surface of the steel bar with epoxy resin AB glue, and a certain thickness of epoxy resin is applied to the highly flexible piezoelectric sensor to protect the piezoelectric ceramic sensor. One end of the wire is connected with a piezoelectric sensor and the other end is connected with a signal generator or a signal receiver. PZT patches were pasted on both sides of the web center of the H-section steel specimen, one for transmitting signals and another one for receiving signals. The experimental device system is shown in Figure 3(a). The H-beam specimen was placed on the electrohydraulic servo test machine. The PZT piece on the left side of the H-beam web was connected to a signal transmitter. The PZT piece on the right of the H-beam web was connected to the signal receiver. To improve the critical load of H-section steel specimens, transverse stiffeners are usually installed in practical engineering applications. H-shaped steel with transverse stiffeners was used in this test, as shown in Figure 3(b). The sampling frequency and sampling time were 7160 Hz and 0.008 s, respectively.

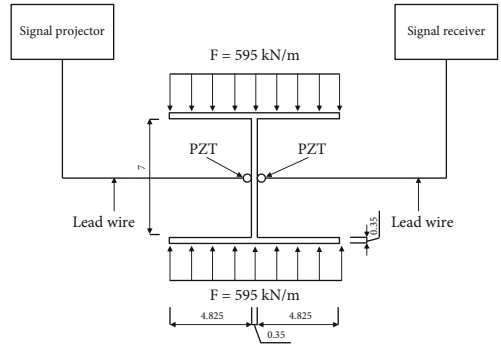


Figure 2: Schematic diagram of H-beam experimental device (unit: cm).

*3.2. Experimental Procedure.* In this test, we studied H-shaped steel members in Groups A and B under two different working conditions; the variables of Groups A and B were load and web height, respectively, as shown in Table 2. The relevant parameters of H-shaped steel are shown in Table 3. In Group A, the webs of H-beams were all 10 cm in height and 3.5 mm thick, and the loads were 200 kN/m, 500 kN/m, and 675 kN/m, respectively. Loads were added from zero to a predetermined value before being removed; the process was repeated (similar to pulse loads). Multiple specimens in each group were loaded and data were collected.A schematic diagram of the experimental device is shown in Figure 4 (taking 675 kN/m as an example; other load groups were similar). In Group B, the thickness of the H-shaped steel member was 3.5 mm, and the web heights were 7 cm, 10 cm, and 13 cm, respectively. Group B applied the same loading steps as Group A, to load H-beam members until buckling occurred. A schematic diagram of each experimental device is shown in Figure 5 (where 13 cm is taken as an example; other web height groups were similar).

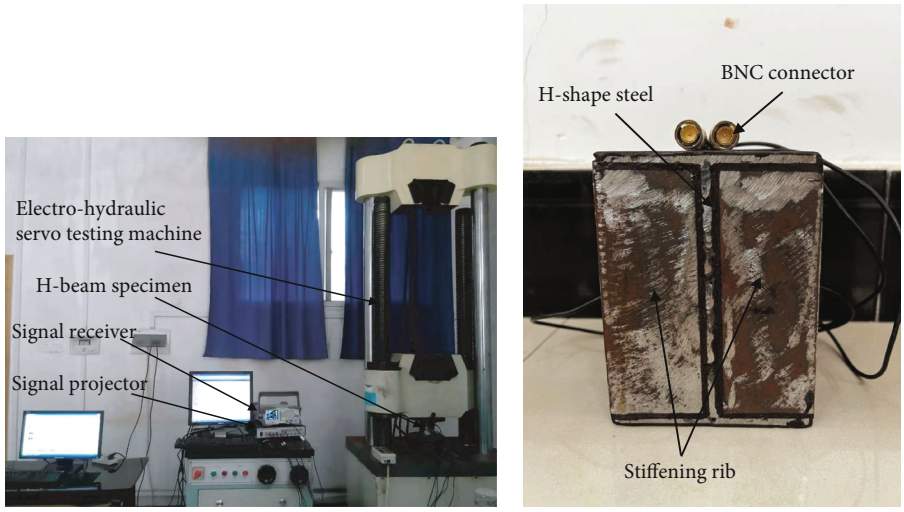


(a) (b)

Figure 3: (a) H-beam stress monitoring experimental system (b) H-shape steel with transverse stiffening rib.

Table 2: Test cases for groups A and B.

| | | | | |
|---|---|---|---|---|
| Group A | Working condition | 1 | 2 | 3 |
| | Load (kN/m) | 200 | 500 | 675 |
| Group B | Working condition | 1 | 2 | 3 |
| | Web height (cm) | 7 | 10 | 13 |

Table 3: Material properties of H-shaped steel.

| Property | Value |
|---|---|
| Density (g/cm$^3$) | 7.85 |
| Young's modulus (Gpa) | 200 |
| Yield strength (Mpa) | 235 |
| Poisson ratio | 0.3 |
| Tensile strength (Mpa) | 450 |
| Linear expansion coefficient of material (1/°C) | 1.20E$^{-05}$ |

Before loading each component, a group of signals including environmental noise and other influences was measured as the control group. These signals are shown in Figure 6. During each experiment, the transmitter emitted the same sinusoidal signal, and the receiver began to receive it. Using the signal received by the signal receiver, the stress of the H-beam was represented. The postbuckling picture of the H-beam is shown in Figure 7 .The PZT response signal was recorded by the data acquisition system, as shown in Figure 3(a).

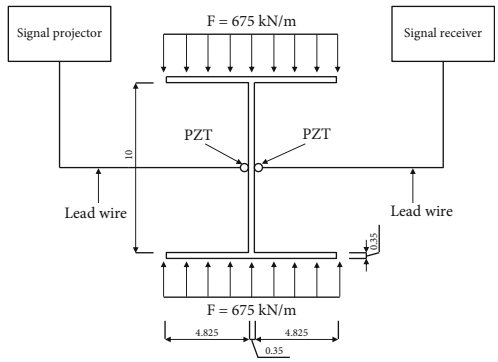


Figure 4: Schematic diagram of experimental device for group A (unit: cm).

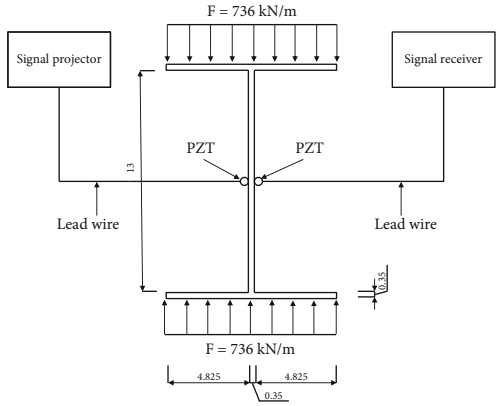


Figure 5: Schematic diagram of experimental device for group B (unit: cm).

## 4. Experimental Results and Discussion

To quantitatively evaluate the attenuation of stress wave energy, the energy exponents of all tested signals in Groups A and B were calculated according to Equations (1) and (2).

Figure 8 shows the time-domain waveform received by the ceramic piezoelectric sensor under different load conditions (Group A). The sampling time of the signal receiver

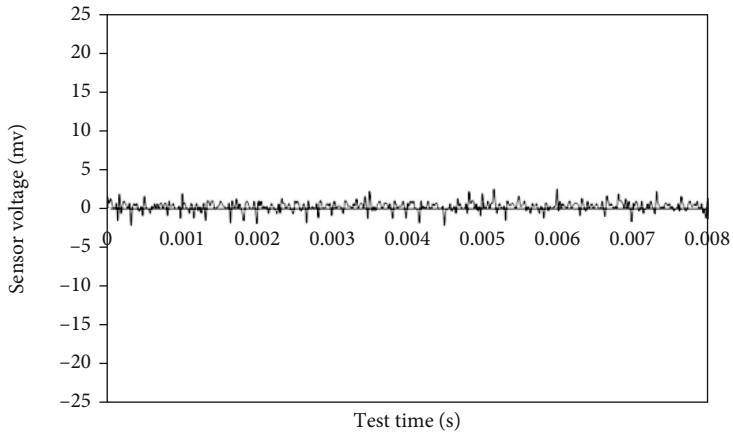


Figure 6: Signal response under the influence of environmental noise.

was 0.008 s. As shown in Figure 8, under Group A working conditions, the signal amplitude received by the signal receiver increased with the load. When the load was 200 kN/m, the time-domain waveform signal amplitude was 225 mv, and the time-domain waveform energy index was 21.3733 $v^2$. When the load was 500 kN/m, the time-domain waveform amplitude was 328 mV, and the time-domain waveform energy index was 28.1223 $v^2$. When the load was 675 kN/m, the time-domain waveform signal amplitude was 364 mv, and the time-domain waveform energy index was 34.7189 $v^2$. From these data, it can be seen that when the load value was below 500 kN/m, the time domain waveform amplitude is increased by ~34.3% and the time domain waveform energy index is increased by ~10.5% when the load value increased by 100 kN/m. When the load value was greater than 500 kN/m and less than 675 kN/m (yield load), the average increase of 100 kN/m increased the amplitude of the time domain waveform energy by ~20.6% and the time domain waveform energy index by ~13.4%. This is because when the H-beam web was subjected to a large load, its internal atomic gap was reduced, and the signal transmitted by the signal transmitter underwent slight attenuation during propagation.

Figure 9 shows the time domain waveform received by the ceramic piezoelectric sensor under different web height conditions (Group B). The sampling time of the signal receiver was 0.008 s. As can be seen from Figure 9, when loads were added to the buckling load, the signal amplitude received by the signal receiver increased under the increase of the H-shaped web height. When the height of the web was 7 cm, the amplitude of the time domain waveform was 264 mv, and the time domain waveform energy index was 27.3267 $v^2$. When the web height was 10 cm, the time domain waveform amplitude was 364 mv, and the time domain waveform energy index was 34.7189 $v^2$. When the web height was 13 cm, the time domain waveform amplitude was 447 mv, and the time domain waveform energy index was 51.2002 $v^2$. From these data, it can be seen that when the ratio between the web height and width was between 0.5 and 1.5, the amplitude of time domain waveform signal

Figure 7: H-shaped steel after buckling.

increased by ~30.5% and the time domain waveform energy index increased by ~14.6% when the web height was increased by 1 cm (on average). This is because when the height of the H-section web increases, the strain at the position of the PZT piece increases after bearing the load; that is, the stress at this position increases. The stress increase causes the iron atoms at that position to bind more tightly; thus, the signal emitted by the signal transmitter decays less during propagation.

## 5. Numerical Verification

To study the strain of H-section steel beams under different load conditions (Group A) and different web height conditions (Group B), this study used ANSYS to establish a finite element model. The web of H-shaped steel (with transverse stiffening ribs) was constrained by flanges on the upper and lower sides and transverse stiffening ribs on the left and right sides; hence, the web could be regarded as a four-sided simply supported plate. These plates were used

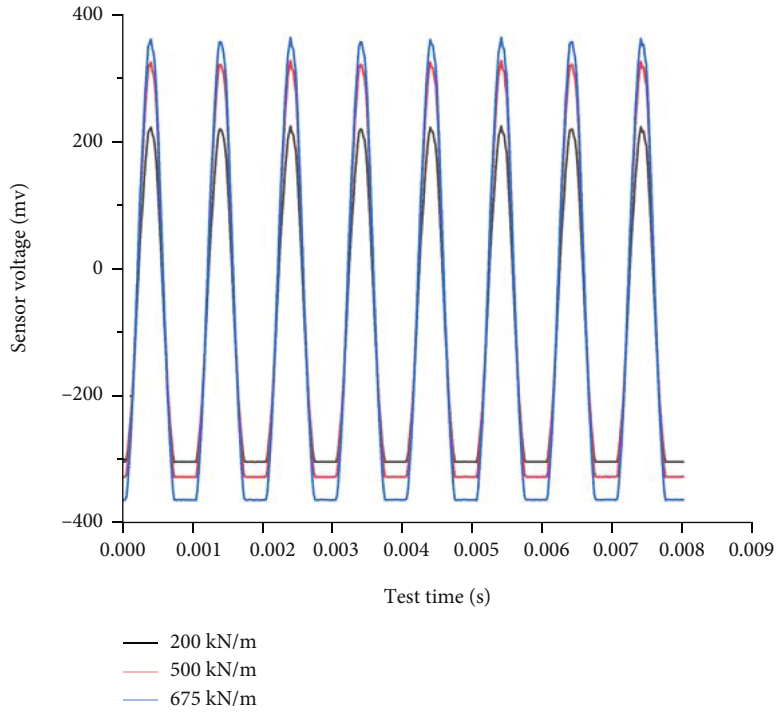


Figure 8: Signal response of each working condition in Group A.

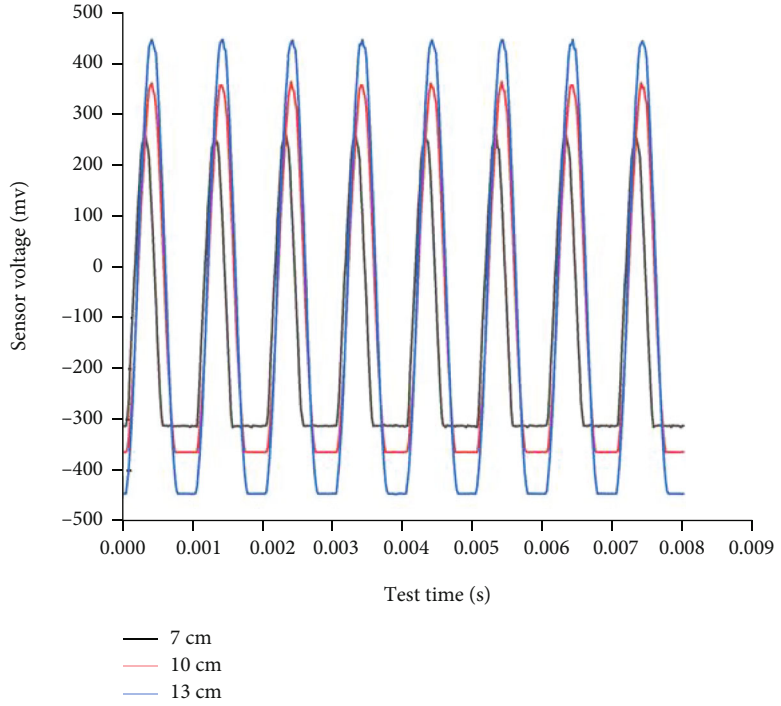


Figure 9: Signal response of each working condition in Group B.

in ANSYS to simulate the web of the H-section steel with transverse stiffening ribs. The force $N_y$ per unit length acted in the $y$ direction, as shown in Figure 10. The material was ideal elastic–plastic, homogeneous, and isotropic, with an elastic modulus of $E = 200$ GPa, a yield strength of $\sigma_s = 235$ Mpa, and a Poisson's ratio of $\nu = 0.3$. Three different web height models were established for the same material coefficient. To observe the postbuckling behavior, the applied load

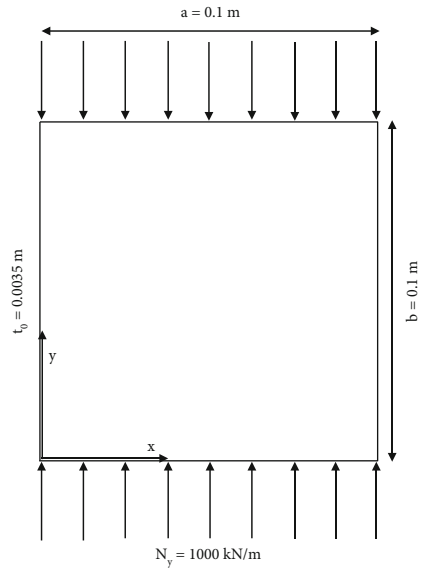


Figure 10: Plan view of a square flat plate (width $a$ = height $b$ = 0.1 m) under in-plane axial compression $Ny$.

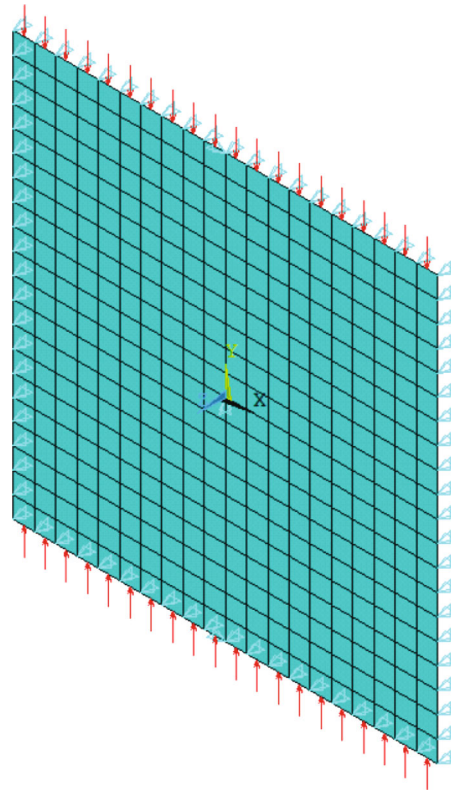


Figure 11: Boundary conditions and loads and meshes.

of each model was set to 1000 kN/m. To constrain the four simply supported plates, a Z-direction constraint was applied thereto. Meanwhile, to eliminate the rigid-body displacement in the $X$ and $Y$ directions, $X$-direction constraints were imposed on the points $x = 0$, $y$ = b/2 and $x = 0$, $y$ = –b/2 and $Y$-direction constraints were imposed on the point $x = 0$, $y = 0$. Finally, a load was applied to the two edges contacting the flange. Load and constraint settings are implemented in ANSYS via SFL, NSEL, and DL command streams. In the finite element simulation, the load is loaded from zero to a predetermined value (monotonically increasing) and the loading step is 1 kN, so the web height of 10 cm model results can reflect the entire A group. Figure 11 presents a schematic of the computational model. The plate adopts a Shell181 unit,

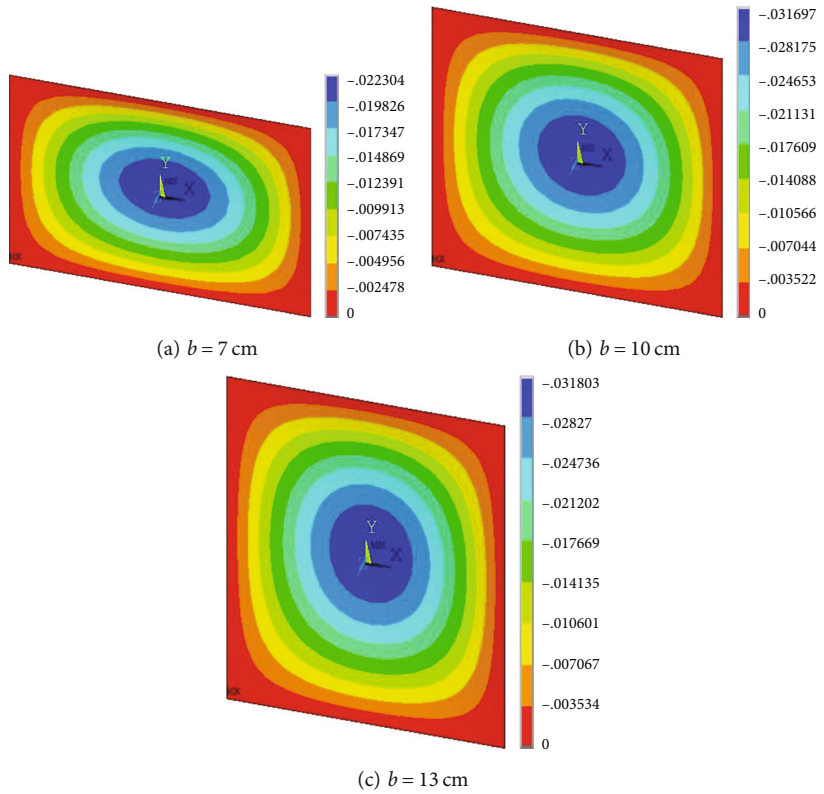


(a) $b = 7$ cm (b) $b = 10$ cm

(c) $b = 13$ cm

Figure 12: First-order modes at different web heights (unit: m).

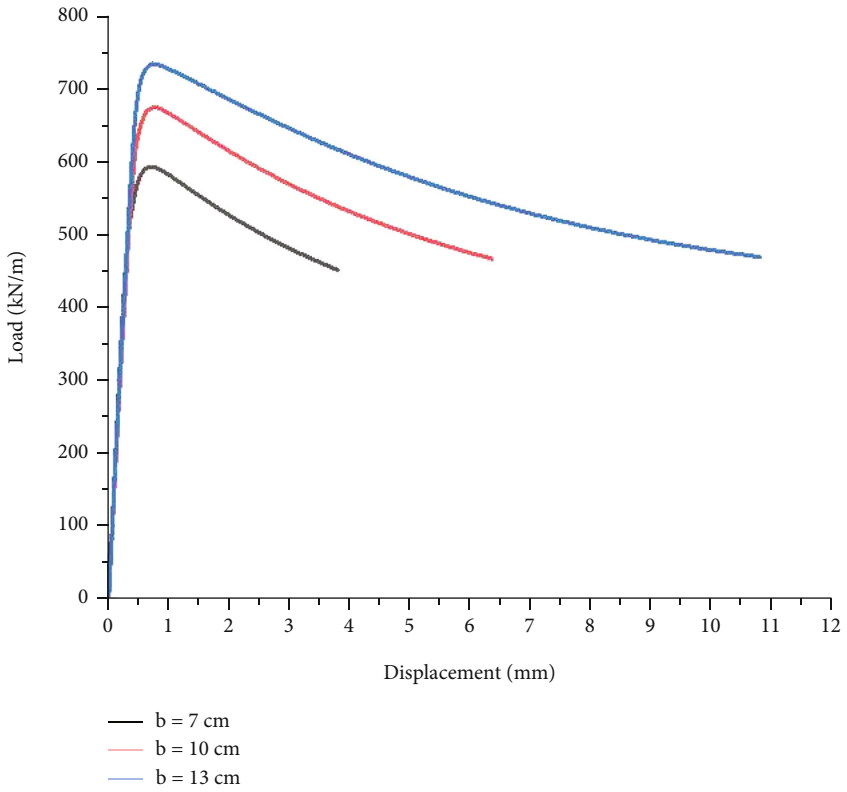


Figure 13: Load displacement curves of each model.

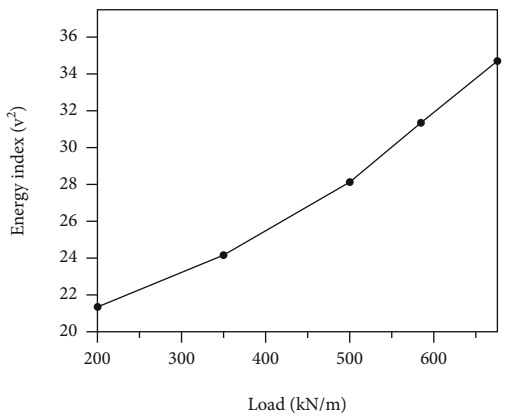


Figure 14: Energy indicator of different loads.

and we selected an appropriate size for grid division. First, the elastic–plastic stiffness matrix and stress–stiffness matrix of the plate were obtained by a static solution; then, the first four orders of buckling modes were obtained via buckling analysis. The first-order buckling modes at three different web heights are shown in Figure 12. When the web thickness was 7 cm, 10 cm, and 13 cm and the external load reached its buckling load, the displacement of the PZT piece was 22.30 mm, 31.69 mm, and 31.80 mm, respectively.

In this study, the displacement $dz$ of the maximum displacement point for the first buckling mode was extracted, and the initial defect was set as $a/50$; then, the defect amplitude ratio $D_0 = a/50/dz$ was applied as the initial defect. The coordinates of each node were updated to alter the geometry of the structure and thereby impose initial defects. The $z$-coordinate value of the center point was $a/50$. Finally, the critical buckling capacity of the plate was solved, and the data for the plate load and its $z$-direction displacement were extracted when the structure was nonlinearly unstable. Figure 13 shows the load displacement curves for the data extracted at three different web heights. The above models indicate that the displacement of the specimen will increase with the increase of the load or the height of the web before it reaches the yield load. As shown in Figure 14, it can be obtained from the experiment that the time domain waveform energy index increases with the increase of the load value. This explains why the signal amplitude received by the ceramic piezoelectric sensor increases with the external load increase.

## 6. Conclusions

To monitor the stress and yield capacity of H-beams, a real-time monitoring method based on the energy signal responses of ceramic piezoelectric sensors was proposed. In this study, different load conditions (Group A) and web height conditions (Group B) were studied. For Group A, when the load value was less than 500 kN/m, the time domain waveform amplitude increased by ~34.3% and the time domain waveform energy index increased by ~10.5% when the load value was increased by 100 kN/m (on average). When the load value exceeded 500 kN/m but was less than 675 kN/m (yield load), the time domain waveform amplitude is increased by ~20.7% and the time domain waveform energy index is increased by ~13.4% for each load value increase of 100 kN/m (on average). For Group B, when the ratio of web height to width was between 0.5 and 1.5, the amplitude of the time domain waveform signal received by the signal receiver increased under the increase in the H-shaped web height. When the web height increased by 1 cm (on average), the time domain waveform amplitude increased by 30.5% and the time domain waveform energy index increased by 14.6%. And by the finite element numerical simulation shows: each group of model before reaching their yield bearing capacity, the load is gradually increasing. To summarize, the energy index value can be used to predict the buckling load value and stress condition when the buckling load value has yet not been reached. Therefore, this study provides a method to detect H-beam stress and evaluate whether H-beams have reached their yield capacity.

## Data Availability

The experimental data used to support the findings of this study are included within the article.

## Conflicts of Interest

The authors declare that they have no conflicts of interest.

## Acknowledgments

The authors acknowledge financial support from the Science and Technology Research Project of Education, Department of Jiangxi Province, in 2019 (Grant No. GJJ190497), as well as the Research Project for High-level Talents from the Jiangxi University of Science and Technology (Grant No. jxncbs19009).

## References

[1] Q. Cao, H. Jiang, and H. Wang, "Shear behavior of corrugated steel webs in H shape bridge girders," *Mathematical Problems in Engineering*, vol. 2015, Article ID 796786, 15 pages, 2015.

[2] R. Feng, H. Zhan, S. Meng, and J. Zhu, "Experiments on H-shaped high-strength steel beams with perforated web," *Engineering Structures*, vol. 177, pp. 374–394, 2018.

[3] S. C. Lee, J. S. Davidson, and C. H. Yoo, "Shear buckling coefficients of plate girder web panels," *Computers and Structures*, vol. 59, no. 5, pp. 789–795, 1996.

[4] S. C. Lee and C. H. Yoo, "Experimental study on ultimate shear strength of web panels," *Journal of Structural Engineering*, vol. 125, no. 8, pp. 838–846, 1999.

[5] E. Ellobody, "Interaction of buckling modes in castellated steel beams," *Journal of Constructional Steel Research*, vol. 67, no. 5, pp. 814–825, 2011.

[6] T. Zirakian and H. Showkati, "Distortional buckling of castellated beams," *Journal of Constructional Steel Research*, vol. 62, no. 9, pp. 863–871, 2006.

[7] N. M. Okasha and D. M. Frangopol, "Integration of structural health monitoring in a system performance based life-cycle

bridge management framework," *Structure and Infrastructure Engineering*, vol. 8, no. 11, pp. 999–1016, 2012.

[8] R. L. Wang, H. Gu, Y. L. Mo, and G. Song, "Proof-of-concept experimental study of damage detection of concrete piles using embedded piezoceramic transducers," *Smart Materials and Structures*, vol. 22, no. 4, article 042001, 2013.

[9] R. L. Lucena and J. M. C. Dos Santos, "Structural health monitoring using time reversal and cracked rod spectral element," *Mechanical Systems and Signal Processing*, vol. 79, pp. 86–98, 2016.

[10] G. Song, W. Li, B. Wang, and S. Ho, "A review of rock bolt monitoring using smart sensors," *Sensors*, vol. 17, no. 4, p. 776, 2017.

[11] Q. Feng, Q. Kong, L. Huo, and G. Song, "Crack detection and leakage monitoring on reinforced concrete pipe," *Smart Materials and Structures*, vol. 24, no. 11, article 115020, 2015.

[12] H. Xin, L. Cheng, R. Diender, and M. Veljkovic, "Fracture acoustic emission signals identification of stay cables in bridge engineering application using deep transfer learning and wavelet analysis," *Advances in Bridge Engineering*, vol. 1, no. 1, pp. 1–16, 2020.

[13] X. Chen, J. Li, G. Zhang, and Y. Shi, "PZT nanoactive fiber composites for acoustic emission detection," *Advanced Materials*, vol. 23, no. 34, pp. 3965–3969, 2011.

[14] L. Cheng, H. Xin, R. M. Groves, and M. Veljkovic, "Acoustic emission source location using Lamb wave propagation simulation and artificial neural network for I-shaped steel girder," *Construction and Building Materials*, vol. 273, article 121706, 2021.

[15] H. Nick, A. Aziminejad, M. H. Hosseini, and K. Laknejadi, "Damage identification in steel girder bridges using modal strain energy-based damage index method and artificial neural network," *Engineering Failure Analysis*, vol. 119, article 105010, 2021.

[16] S. Tohidi and Y. Sharifi, "Neural networks for inelastic distortional buckling capacity assessment of steel I-beams," *Thin-Walled Structures*, vol. 94, pp. 359–371, 2015.

[17] Z. Zhou, B. Zhang, K. Xia, X. Li, G. Yan, and K. Zhang, "Smart film for crack monitoring of concrete bridges," *Structural Health Monitoring*, vol. 10, no. 3, pp. 275–289, 2011.

[18] B. Glisic and D. Inaudi, "Development of method for in-service crack detection based on distributed fiber optic sensors," *Structural Health Monitoring*, vol. 11, no. 2, pp. 161–171, 2012.

[19] F. Raeisi, A. Mufti, B. Algohi, and D. J. Thomson, "Placement of distributed crack sensor on I-shaped steel girders of medium-span bridges, using available field data," *Structural Control and Health Monitoring*, vol. 26, no. 10, article e2432, 2019.

[20] S. Park, S. Ahmad, C. B. Yun, and Y. Roh, "Multiple crack detection of concrete structures using impedance-based structural health monitoring techniques," *Experimental Mechanics*, vol. 46, no. 5, pp. 609–618, 2006.

[21] D. Ai, H. Zhu, H. Luo, and J. Yang, "An effective electromechanical impedance technique for steel structural health monitoring," *Construction and Building Materials*, vol. 73, pp. 97–104, 2014.

[22] J. Zhang, Y. Huang, and Y. Zheng, "A feasibility study on timber damage detection using piezoceramic-transducer-enabled active sensing," *Sensors*, vol. 18, no. 1563, pp. 1–11, 2018.

[23] T. Jiang, Q. Kong, Z. Peng et al., "Monitoring of corrosion-induced degradation in prestressed concrete structure using embedded piezoceramic-based transducers," *IEEE Sensors Journal*, vol. 17, no. 18, pp. 5823–5830, 2017.

[24] S. H. Choy, X. P. Jiang, K. W. Kwok, and H. L. W. Chan, "Piezoelectric and dielectric characteristics of lead-free BNKLBT ceramic thick film and multilayered piezoelectric actuators," *Ceramics International*, vol. 36, no. 8, pp. 2345–2350, 2010.

[25] D. Wang and H. Zhu, "Monitoring of the strength gain of concrete using embedded PZT impedance transducer," *Construction and Building Materials*, vol. 25, no. 9, pp. 3703–3708, 2011.

[26] G. Park, H. H. Cudney, and D. J. Inman, "Feasibility of using impedance-based damage assessment for pipeline structures," *Earthquake Engineering & Structural Dynamics*, vol. 30, no. 10, pp. 1463–1474, 2001.

[27] F. Wang, S. C. M. Ho, L. Huo, and G. Song, "A novel fractal contact-electromechanical impedance model for quantitative monitoring of bolted joint looseness," *IEEE Access*, vol. 6, pp. 40212–40220, 2018.

[28] C. Rosalie, A. Chan, W. K. Chiu, S. C. Galea, F. Rose, and N. Rajic, "Structural health monitoring of composite structures using stress wave methods," *Composite Structures*, vol. 67, no. 2, pp. 157–166, 2005.

[29] G. Du, Q. Kong, H. Zhou, and H. Gu, "Multiple cracks detection in pipeline using damage index matrix based on piezoceramic transducer-enabled stress wave propagation," *Sensors*, vol. 17, no. 8, 2017.